



Evading Strength-Ductility Tradeoff in Mg Alloy via Uniform Microstructure and Unique Texture Modification Induced by Moderate Temperature ECAP

Hongfei Zhang^{1,2} · Jian Lei^{1,2} · Yutian Ding^{1,2} · Yubi Gao^{1,2} · Ruimin Li^{1,2} · Yue Shen^{1,2}

Received: 23 September 2022 / Accepted: 10 November 2022 / Published online: 26 December 2022
© The Author(s) under exclusive licence to The Korean Institute of Metals and Materials 2022

Abstract

Tweaking the distribution of grains, precipitates, and texture components is a successful strategy employed to enhance the strength and formability of Mg alloys. Herein, moderate temperature equal channel angular pressing (ECAP) deformation was employed to control the microstructure and tune the corresponding mechanical properties of the Mg–6Zn–1Mn alloy. The analysis results indicated a uniform distribution of grains and second phases. The original strong basal texture of the extruded Mg–6Zn–1Mn alloy was disintegrated, and a weak basal texture gradually developed after 2 passes of ECAP deformation. The fine grains, second phases, and high-density dislocations provide high strength to the alloy, with contributions of 105.1 MPa, 47.1 MPa and 78.8 MPa, respectively. The excellent ductility (20.6%) is mainly attributed to the weak basal texture and high Schmid factor of prismatic $\langle a \rangle$ slip. The 2P sample exhibits good strength-ductility synergy effects with a value of $YS \times EL$ equal to 5.8. The results indicate that moderate temperature ECAP deformation can enable the formation of a uniform microstructure and unique texture to enhance the mechanical properties of the Mg–6Zn–1Mn alloy.

Keywords Mg–6Zn–1Mn alloy · Moderate temperature ECAP · Strength-ductility synergy · Uniform microstructure · Weak basal texture

1 Introduction

As a conventional method for enhancement the mechanical properties of Mg alloys, the extrusion deformation has been attracted increasing attention in recent years [1–5]. Especially, extruded Mg rods are an important component among the most of Mg products, and acted as an intermediate billet in the fabrication of engineering component, such as biodegradable medical devices, aerospace components, military hardware, and automotive parts [6, 7]. To maximize subsequent processing of the materials, adequate deformability and strength are essential [6]. However, owing to the formation of strong basal texture, extruded Mg rods generally

exhibit high strength but relatively poor ductility, which is detrimental to the deformation capacity [8].

Recently, extensive investigations have been conducted on the modification of basal texture to enhance the ductility of Mg alloys [6, 9–13]. Pei et al. demonstrated that the co-segregation of Al, Zn, and Ca atoms results in the preferential growth of non-basal grains and therefore contributes to texture modification in AZW and AZX alloy during recrystallization [9]. Yan et al. prepared high yield strength (YS, 130 MPa) and high elongation (EL, 40%) dilute quaternary Mg–0.8Zn–0.3Gd–0.2Ca (wt%) with a circular non-basal texture via rolled heat-treatment [11]. Tong et al. reported that grain refinement and texture modification using ECAP led to an increase in the YS [14]. Compared with traditional methods, such as heat treatment and the addition of rare earth elements, ECAP is considered the most commonly used technology for weakening the basal texture, generating a non-basal texture, and thereby improving ductility [8, 14]. Furthermore, ECAP can produce small-sized grain and uniformly distributed second phases [15–18]. Despite these advantages, the application of ECAP is limited by the decrease in the YS as the number of deformation passes

✉ Yutian Ding
dingyt@lut.edu.cn

¹ State Key Laboratory of Advanced Processing and Recycling of Nonferrous Metals, Lanzhou University of Technology, Lanzhou 730050, People's Republic of China

² School of Materials Science and Engineering, Lanzhou University of Technology, Lanzhou 730050, People's Republic of China

increase [19–21]. This can be mainly attributed to the formation of the non-basal texture with high SF after ECAP. Therefore, diminishing texture softening, and maximizing the benefits of microstructure refinement, are challenging for the ECAP of Mg alloys. Generally, to obtain an excellent microstructure refinement, the ECAP temperature must be relatively low. The lack of operative slip systems and sharp basal textures in the extruded rod easily lead to the frequent occurrence of cracks in the ECAP shearing deformation [12]. Moreover, an excessively high processing temperature results in a relatively low strength, owing to the formation of large grains and low dislocation density [13, 22]. Therefore, it is necessary to control the microstructure and corresponding mechanical properties of Mg alloys via moderate temperature ECAP deformation.

Herein, to determine the effects of moderate temperature ECAP on Mg alloys, a cost-effective Mg–6Zn–1Mn alloy was selected as the starting material [23, 24], and low temperature extrusion and 4 passes of moderate temperature ECAP deformation were performed on the alloy. The microstructural evolution and mechanical properties of the samples were studied. The results are expected to serve as guidelines for preparing Mg alloys with high strength-ductility synergy.

2 Experimental methods

2.1 Casting, extrusion, and ECAP deformation

In the current study, the Mg–6Zn–1Mn (wt%) alloy was fabricated using high-purity Mg (99.99%), Zn (99.99%), and Mn (99.95%) in specific proportions in a vacuum induction furnace in an argon protective atmosphere. First, the pure Mg, Zn, and Ca were simultaneously added to the furnace. After Mg was completely melted, the melt was held at 760–780 °C for 10 min, the melt was poured into a copper mould with 105 mm diameter and 310 mm high when the temperature decreased to 720 °C–740 °C. Screens with 8 and 20 mesh were placed on top of the copper mould to obstruct impurities. The specific chemical composition of the alloy was determined using inductively coupled plasma optical emission spectrometry (Agilent 5110 ICP-OES), and the results are listed in Table 1.

After homogenization treatment at 420 °C for 24 h, an ingot with a diameter of 39 mm was obtained from the homogenized billet. Before extrusion, the sample and die were heated to 260 °C for 30 min. Subsequently, the hot

extrusion process was conducted with an extrusion ratio of 11:1 and extrusion speed of ~5 mm/s. Finally, a rod with a diameter of 12 mm was obtained. The as-extruded samples were then processed via 1 to 4 passes of ECAP deformation using an ECAP die. The sample and die were preheated to 300 °C before each pass of the ECAP deformation. A mixture of graphite and high temperature lubricating oil was used as a lubricant in the extrusion and ECAP deformation. The choice of deformation temperature can refer to the analysis of hot compression deformation behavior and the processing map of the Mg–6Zn–1Mn alloy [25]. When the deformation temperature exceeded 325 °C, dynamic recrystallization (DRX) occurred easily. Therefore, the ECAP process in this study can be named as moderate temperature deformation. Owing to the moderate temperature, we define the extrusion as low temperature process. The interior and exterior channel angles of the die were 120° and 60°, respectively. Route Bc (the rotated angle for the sample between adjacent passes is 90° in the same direction) was adopted, with a punch speed of ~15 mm/s. Table 2 lists the codes of samples with different processing states.

2.2 Microstructure and mechanical properties

The microstructures of the samples were investigated using optical microscopy (OM, ZEISS Axio Scope A1) and scanning electron microscopy (SEM, FEI Quanta FEG 450) equipped with electron backscattering diffraction (EBSD). Deformed alloys with surfaces parallel to the extrusion direction (ED) or ECAP direction (ED) were observed. The OM and SEM samples were etched in an alcohol solution containing 5% nitric acid. The specimens for EBSD observation were polished mechanically and then electrochemically using a solution of 60 vol% ethanol, 15 vol% glycerine, and 25 vol% phosphoric acid. EBSD characterization was performed at an operating voltage of 20 kV, with a step size range of 0.15 µm. Channel 5 software was used for the data

Table 2 The treated processes of the specimens and the corresponding specimen names

| Treated processes | Specimen names |
|----------------------|----------------|
| As-extruded (0 pass) | Ex |
| ECAP-1 pass | 1P |
| ECAP-2 pass | 2P |
| ECAP-4 pass | 4P |

Table 1 Chemical composition of Mg–6Zn–1Mn alloy in this study

| Element | Zn | Mn | Fe | Ni | Cu | Mg |
|---------|------|------|-------|--------|--------|-----|
| wt% | 5.97 | 0.96 | 0.001 | 0.0011 | 0.0007 | Bal |

analysis. The geometrically necessary dislocations (GNDs) were calculated using the following equation [3]:

$$\rho_{GND} = \frac{2\Theta}{\mu b}$$

where b is the Burgers vector (~ 0.32 nm) for Mg alloys, μ is the unit length of the circuit around a specific point of interest (150 nm, which is equal to the scanning step length), and Θ represents the local misorientation.

Dog-bone-shaped tensile specimens with a gauge length of 20 mm, a width of 2 mm, and a thickness of 8 mm were tested by a testing machine (AGS-X) with a tensile speed of 0.3 mm/min at room temperature. And at least three specimens for each condition were tested. The tensile fracture morphologies were observed using SEM.

3 Results

3.1 Microstructure

Figure 1 presents the OM and SEM microstructures of the as-cast and homogenized samples. The as-cast alloy exhibits a typically coarse equiaxed grain structure with second phases distributed along grain boundaries (GBs) and within the grains (Fig. 1a, b). According to the point of energy dispersive spectroscopy (EDS) analysis, the atomic ratios of Zn and Mg at positions 1 and 2 are 1.68 and 1.82, respectively (Table 3). Therefore, these particles are determined to be

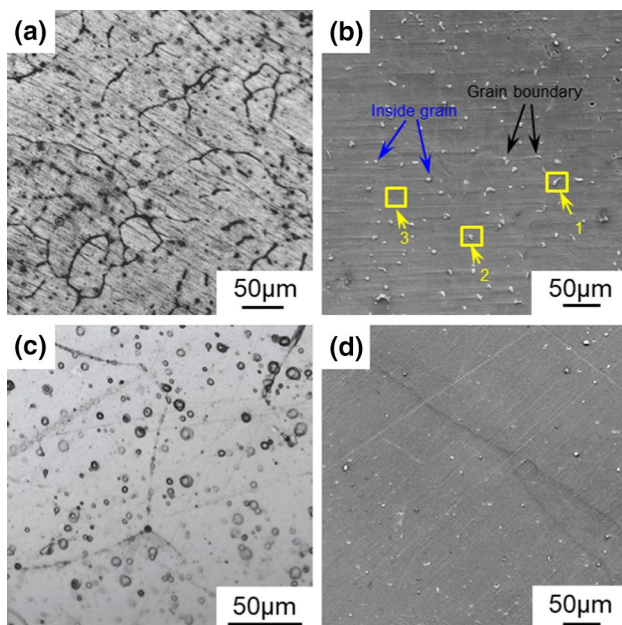


Fig. 1 The OM (a, c) and SEM (b, d) images of as-cast (a, b) and as-homogenized (c, d) Mg–6Zn–1Mn alloys

Table 3 The point of EDS analysis for the second phase particles and the matrix

| | Mg (at%) | Zn (at%) | Mn (at%) |
|---|----------|----------|----------|
| 1 | 37.2 | 62.6 | 0.2 |
| 2 | 35.4 | 64.5 | 0.1 |
| 3 | 99.6 | 0.4 | 0.0 |

the MgZn₂ phases. The Mn concentration is maintained at a low level in the phases. Mn acts as a heterogeneous nucleation site for the second phases in Mg alloys, and promotes precipitation from the Mg matrix [26]. Moreover, almost no Zn and Mn are detected in the Mg matrix (point 3), which is mainly attributed to the low solid solubility of these elements in the Mg matrix at room temperature [26]. The characterization in Fig. 1c shows no significant difference between grains with or without homogenization. However, most of the second phases melt into the Mg matrix after homogenization treatment, as shown in Fig. 1d. This can be further confirmed by the EDS mappings analysis in Fig. 2, and the most of Mn element distribute at GBs.

Figure 3 shows the SEM microstructure of the samples prepared by extrusion and the subsequent 1, 2, and 4 passes of ECAP deformation. As shown in Fig. 3a, numerous second phase particles are elongated and distributed along the ED. With an increase of ECAP passes, the size of the second phase gradually decreases. Especially after 2 and 4 passes of ECAP, the average size of the second phase can reach the sub-micro scale. This indicates that ECAP deformation can break the coarse intermetallic compounds (IMCs), facilitating a uniform distribution. According to the grain size statistics in Fig. 4, the as-extruded alloy contains numerous fine grains with sizes less than 1 μm, and the average grain

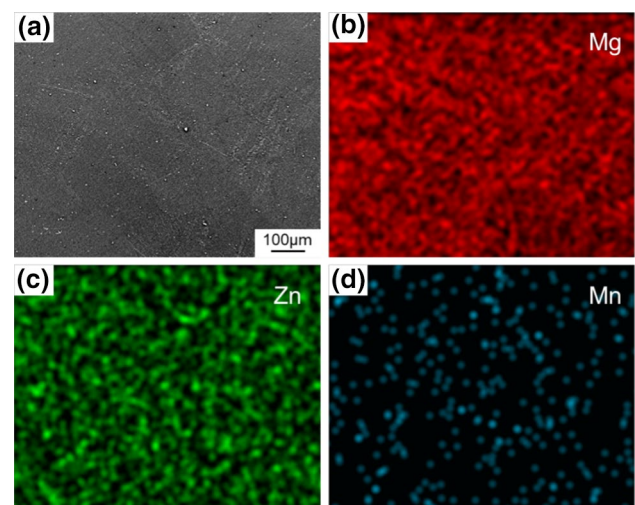


Fig. 2 The EDS mappings of as-homogenized Mg–6Zn–1Mn alloy

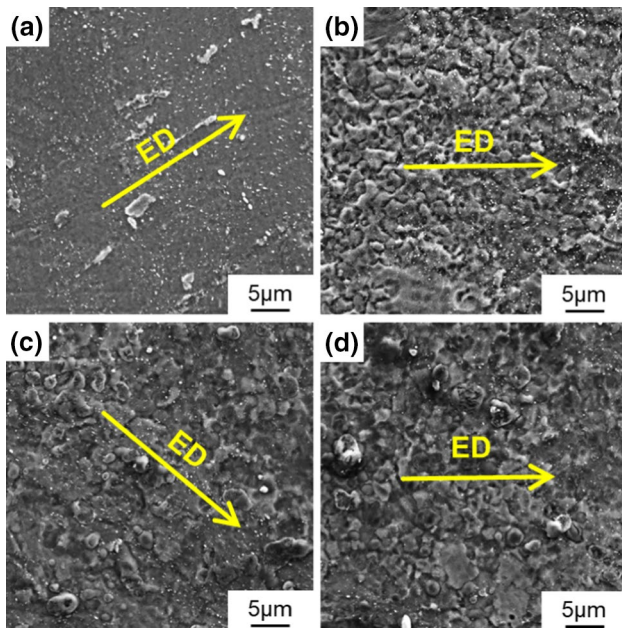


Fig. 3 The SEM image of deformed Mg–6Zn–1Mn alloys: **a** Ex; **b** 1P; **c** 2P; **d** 4P

size is 1.12 μm . Further deformation causes a slight increase in the grain size with the average value of 1.57 μm (1P sample). After 2 passes ECAP deformation, the average grain size significantly increases by ~ 0.7 μm , compared to that of the 1P sample. The average grain size of the 4P sample is 2.016 μm , which is basically equivalent to that of the Mg alloy processed by 2 passes of ECAP deformation.

3.2 Grain and texture evolution

Figure 5 shows the orientation image microscopy (OIM) images of the Mg–6Zn–1Mn alloy derived from EBSD analysis. 15° is considered to be the threshold of low-angle GB (LAGB, white line). The reference direction is the normal direction (ND). The pure red, blue, and green colours represent the $\langle 0001 \rangle$, $\langle 10\text{-}10 \rangle$, and $\langle 11\text{-}20 \rangle$ crystallographic directions parallel to the ND, respectively. Grains with a $\langle 0001 \rangle // \text{ND}$ orientation indicate that the basal plane is parallel to the ED, which corresponds to the basal texture. Figure 5a shows that the as-extruded alloys have a heterogeneous grain structure, including small and large elongated

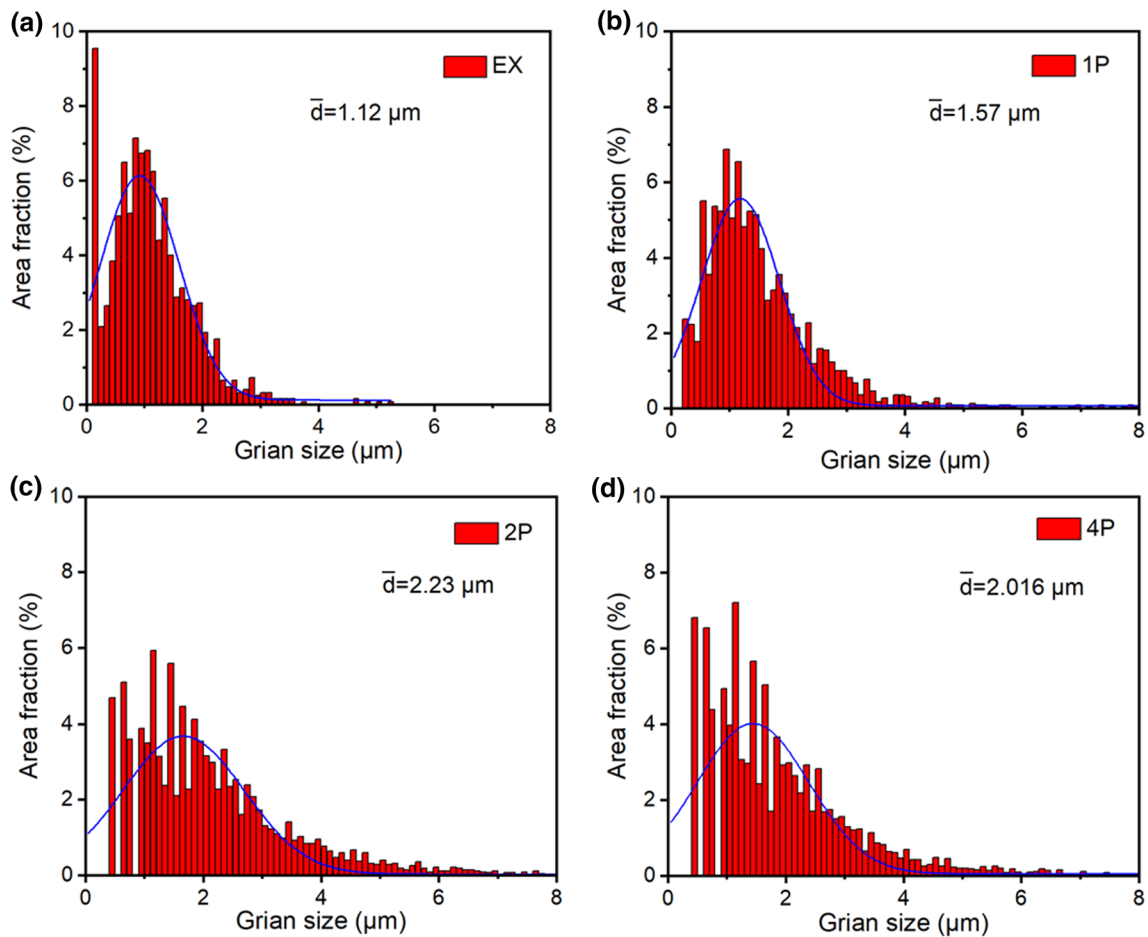


Fig. 4 Grain size statistics of deformed Mg–6Zn–1Mn alloys: **a** Ex; **b** 1P; **c** 2P; **d** 4P

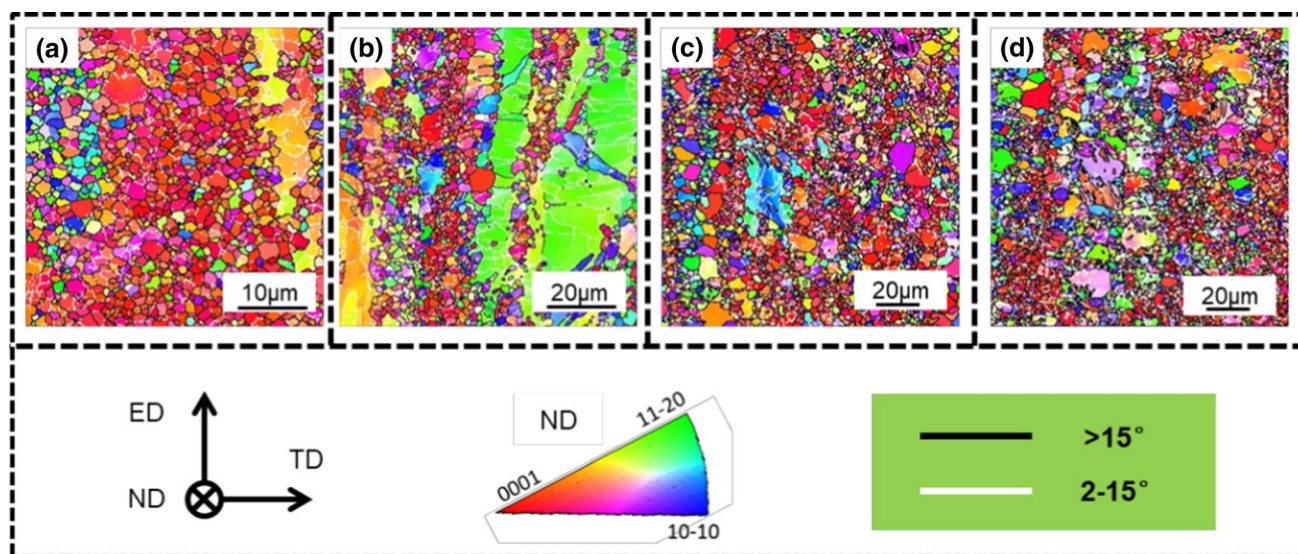


Fig. 5 OIM of the deformed Mg–6Zn–1Mn alloys: **a** Ex; **b** 1P; **c** 2P; **d** 4P

grains. Most grains exhibit a $\langle 0001 \rangle // \text{ND}$ orientation, implying a remarkable basal texture component. With further deformation, the number of grains with the $\langle 0001 \rangle // \text{ND}$ orientation significantly decreases in the 1P sample, and most of grains exhibit the $\langle 11\text{-}20 \rangle // \text{ND}$ orientation. After 2 passes of deformation, the elongated grains in the 1P samples are significantly broken, and most grains exhibit $\langle 0001 \rangle // \text{ND}$ orientation. As observed, the orientation of the 4P sample is similar to that of the 2P alloy. The evolution of the grain orientation is related to shear-induced DRX during ECAP deformation. More importantly, fine grains with the $\langle 0001 \rangle$ direction parallel to the transverse direction (TD) can play an important role in mechanical properties through texture modification. Actually, the TD and ND are equivalent for the extrusion bar, indicating that a similar effect may exist for fine grains with $\langle 0001 \rangle // \text{ND}$ orientation in this study.

Figure 6 shows the texture evolution of the Mg–6Zn–1Mn alloy processed by extrusion and 1, 2, and 4 pass deformation. The as-extruded sample shows a strong basal deformation texture component ($\langle 01\text{-}10 \rangle // \text{ED}$) of $\langle 0001 \rangle // \text{ED}$ with a maximum intensity of 15.63 (Fig. 6a), which is in agreement with the result in Fig. 5a. After 1 pass of ECAP deformation, the 1P sample retains a strong basal deformation texture with an intensity of 22.27 (Fig. 6b). It is worth noting that there also exists another type of texture in the alloy from the (10-10) pole figure. With further deformation, grains with the $\langle 01\text{-}10 \rangle // \text{ED}$ orientation gradually transform to acquire the $\langle \text{-}12\text{-}10 \rangle // \text{ED}$ orientation, indicating the occurrence of the basal recrystallization texture (Fig. 6c). Owing to the effect of DRX, the texture intensity significantly decreases to a value of 5.18. The sample processed by 4 passes of ECAP deformation mainly exhibits a $\langle \text{-}12\text{-}10 \rangle // \text{ED}$ basal

recrystallization texture with a maximum intensity of 5.3, and a weak $\{0001\} \langle 01\text{-}10 \rangle$ texture exists. Therefore, the texture component transforms from $\{0001\} \langle 01\text{-}10 \rangle$ to $\{0001\} \langle \text{-}12\text{-}10 \rangle$ during the deformation.

Figure 7 is the grain orientation distribution function (ODF) sections of the Mg–6Zn–1Mn alloy processed by the extrusion and 1, 2, and 4 passes of ECAP deformation. The ideal ODF diagrams for $\phi = 0^\circ$ and $\phi = 30^\circ$ have been presented in our previous report [27]. The results indicate that the texture evolution tendency is basically consistent with the analysis shown in Fig. 6. Worthy to be noted is that there exists the $\{ \text{-}12\text{-}10 \} \langle 10\text{-}11 \rangle$ texture in the 1P sample. Moreover, the textures observed herein are slightly deviated from the ideal texture component, indicating a basal plane tilt of the texture.

3.3 Mechanical properties

The tensile test results for the Mg–6Zn–1Mn alloy are shown in Fig. 8. As observed, the as-cast alloy exhibits relatively mediocre mechanical properties with YS of ~ 140 MPa, ultimate tensile strength (UTS) of ~ 200 MPa, and EL of $\sim 5.1\%$. After the extrusion deformation, the mechanical properties-YS, UTS, and EL significantly improve to ~ 271 MPa, ~ 312 MPa, and $\sim 9.2\%$, respectively. After 1 pass ECAP deformation, the YS, UTS, and EL for extruded Mg alloy is increased further. With further ECAP deformation, the 2P sample exhibits excellent comprehensive mechanical properties with YS, UTS, and EL values of ~ 282 MPa, ~ 306 MPa, and $\sim 20.6\%$, respectively. With the increase of ECAP pass, the strength of the alloy (4P) remains unchanged, but the ductility decreased obviously. To demonstrate the excellent properties of the Mg–6Zn–1Mn alloy,

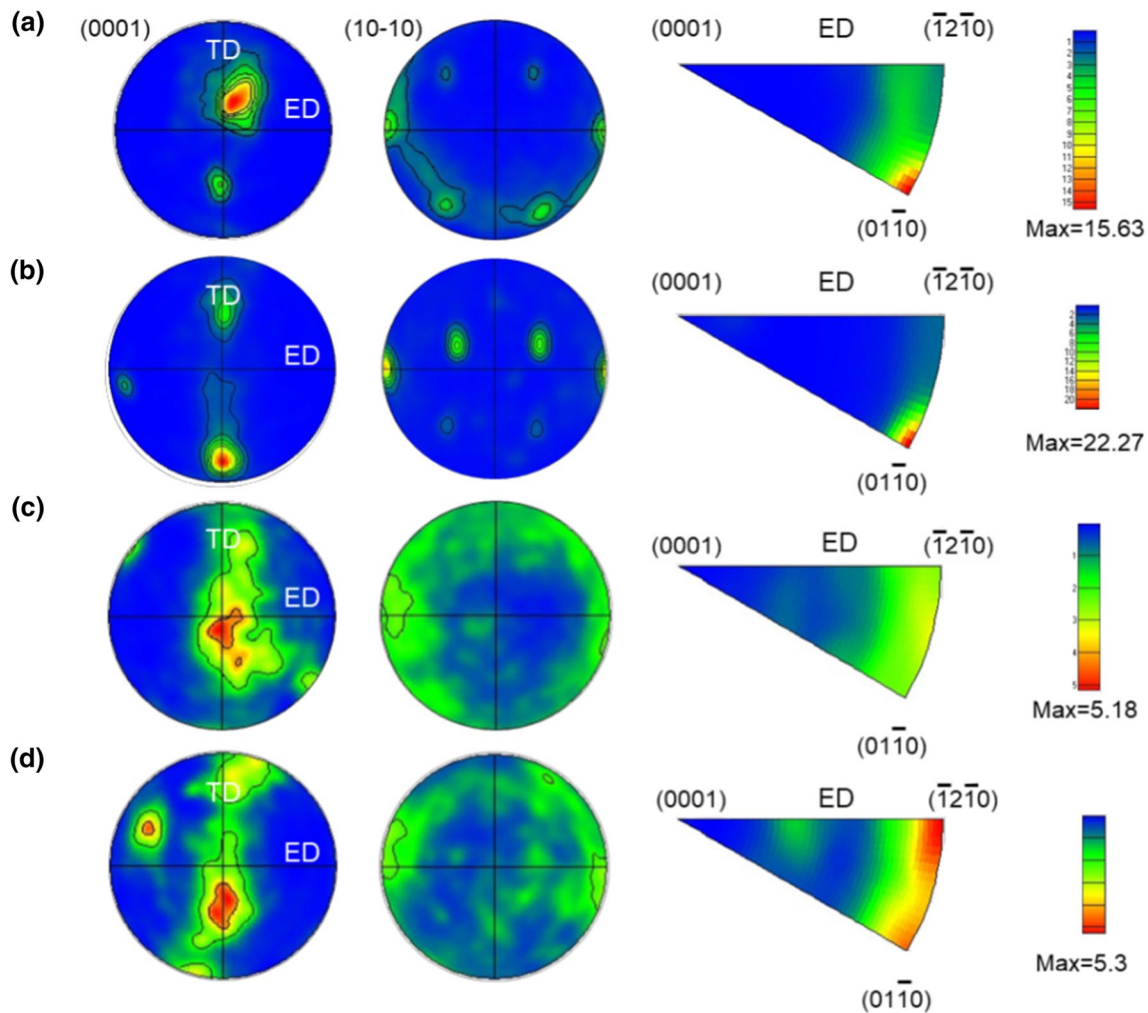


Fig. 6 Pole figures and inverse pole figures of deformed Mg–6Zn–1Mn alloys: **a** Ex; **b** 1P; **c** 2P; **d** 4P

the tensile results from the current study were compared with those of the samples prepared by the same method, and the relevant results are summarized in Fig. 9. It shows the $YS \times EL$ value corresponding to the ECAP passes for various Mg alloys, indicating the 2P sample exhibits an excellent strength-ductility synergy with few deformation passes.

4 Discussion

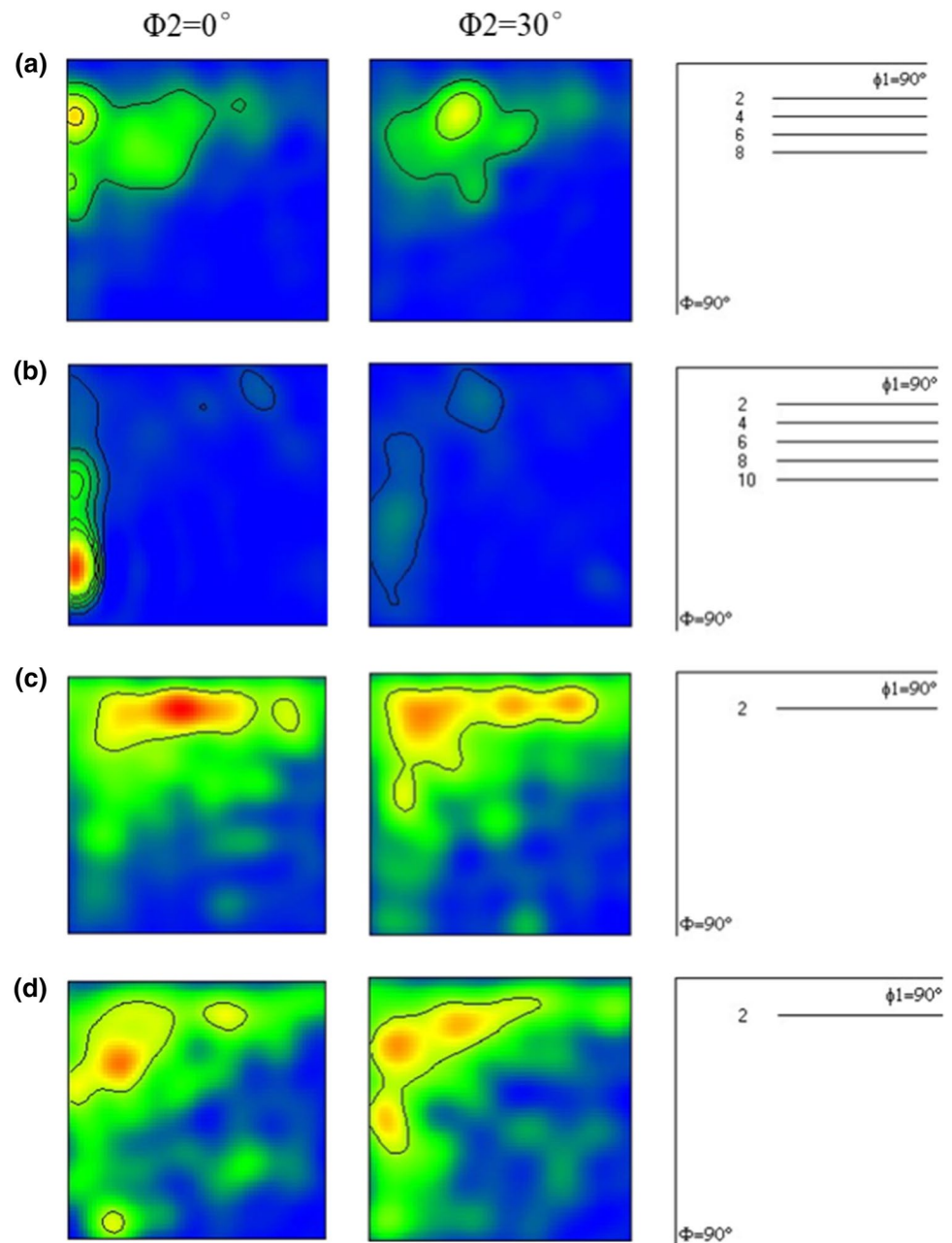
Generally, an excellent combination of strength and ductility is essential to promote the application of Mg alloys. However, an intrinsic tradeoff relationship exists between strength and ductility, which can be attributed to the dislocation slip. Based on the Hall–Petch relationship theory, grain refinement can improve comprehensive mechanical properties to a certain extent. Moreover, other factors, such as the size and distribution of the second phases, texture components, and dislocation density, are critical for fabricating

high-performance Mg alloys. Therefore, it is necessary to tune these inherent microstructures to obtain the strength-ductility synergy in Mg alloys. This study developed Mg alloys with excellent comprehensive mechanical properties via simple 2 pass ECAP deformation. The related microstructural evolution, strengthening, and toughening mechanisms are discussed in subsequent sections.

4.1 Grain evolution mechanism

Figure 10 presents the area fraction statistics of the recrystallized, substructured, and deformed regions of the different samples. As observed, with an increase in the deformation, the number of sub-grains decreases significantly, whereas the number of deformed-grains increases. Among them, the 2P sample exhibits the highest DRX fraction, with a value of $\sim 34\%$. With further ECAP deformation, the fraction of the DRX grains slightly decreases. Microstructure evolution is generally related to the DRX behavior induced by

Fig. 7 ODF sections of deformed Mg–6Zn–1Mn alloys: **a** Ex; **b** 1P; **c** 2P; **d** 4P



the deformation temperature and total strain [22, 31]. The extruded sample has a heterogeneous grain structure owing to the low extrusion temperature and low deformation strain. Many sub-grains or dislocations exist within the grains that did not undergo DRX, exhibiting a high fraction (~47%) of LAGB, as shown in Fig. 11a. With further ECAP deformation, owing to the thermal activation and accumulation of the strains, dynamic recovery and DRX occur, resulting in a decrease in the LAGBs, as shown in Fig. 11b, c. After 4 passes of deformation, the LAGB in the 4P samples slightly increases, which is consistent with the analysis of the DRX behavior in Fig. 10.

Furthermore, DRX images and misorientation angle maps are presented to analyze the mechanism of grain evolution (Fig. 12). As observed, increasing the ECAP to 2 passes, large amount of DRX grains (blue region) are appeared obviously. When reaching to the 4 passes deformation, the deformed grains (red region) slightly increased. According to the previous studies, the DRX mechanism can be effectively identified by evaluating the local and cumulative misorientations in the grains that did not undergo DRX [32, 33]. Along the line drawn in the DRX image, the cumulative misorientation is detected to be larger than 15° for the four samples, whereas the local misorientation are about 5° , indicating the occurrence of continuous dynamic recrystallization

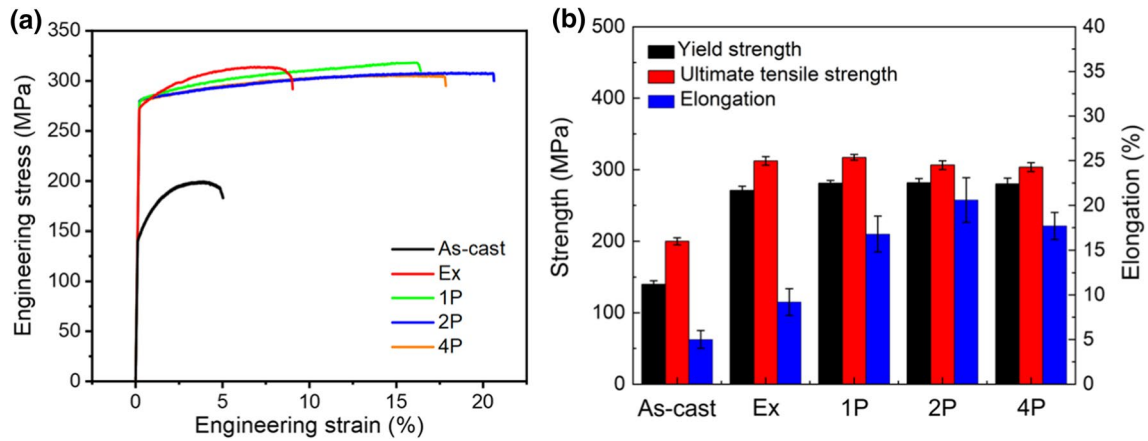


Fig. 8 Mechanical properties of Mg–6Zn–1Mn alloys: **a** engineering stress–strain curves; **b** the tensile test results of the experimental alloys at room temperature

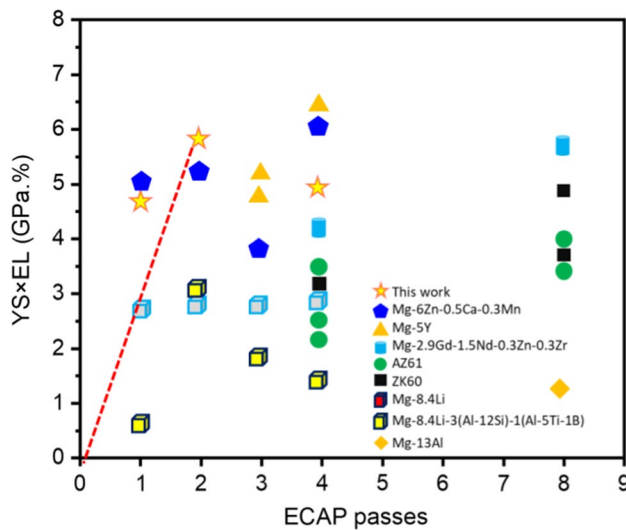


Fig. 9 Comparison of YS×EL versus ECAP passes for present as-deformed Mg–6Zn–1Mn alloy with other Mg alloys [12–14, 20, 28–30]

(CDRX) [32, 33]. This suggests that the new grains are mainly formed by the gradual increase in the misorientation of low angle boundaries. Therefore, CDRX dominates the DRX mechanism during the entire hot deformation, and a schematic of the evolution mechanism is shown in Fig. 13. The process can be divided into three stages. (i) The dislocation tangle appears in grains owing to the effect of dislocation slip in the shear deformation region, particularly the basal slip. The dislocation cell microstructure is subsequently formed (Fig. 13a). (ii) The occurrence of dynamic recovery leads to the formation of sub-grains, as shown in Fig. 13b. (iii) New DRX grains are generated owing to the migration and combination of sub-grains (Fig. 13c).

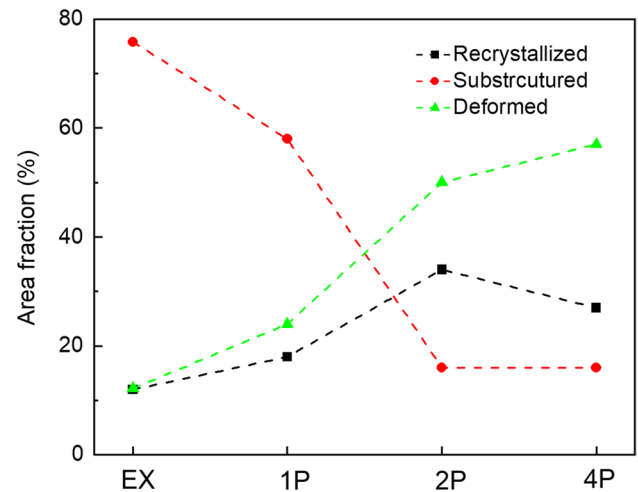


Fig. 10 The area fraction statistic of the recrystallized, substructured and deformed region of Mg–6Zn–1Mn alloys processed with different methods

5 2Texture evolution

Figure 14 is the schematic diagram of the texture evolution for Mg–6Zn–1Mn alloy processed by different methods. The as-extruded alloy exhibits a strong basal fiber texture component with the $\langle 01\text{-}10 \rangle$ direction parallel to the ED (Fig. 14a), which is commonly observed in as-extruded Mg alloys [4, 34]. As shown in Fig. 14b, after 1 pass of ECAP, two types of texture exist: basal fiber texture ($\langle 01\text{-}10 \rangle //$ ED) and non-basal texture ($\{-12\text{-}10\} \langle 10\text{-}11 \rangle$). With further ECAP deformation, the 2P sample transforms to possess conventional basal texture ($\langle 01\text{-}10 \rangle //$ ED and $\langle -12\text{-}10 \rangle //$ ED), as shown in Fig. 14c. This phenomenon has rarely been reported for Mg–Zn series alloys processed by ECAP

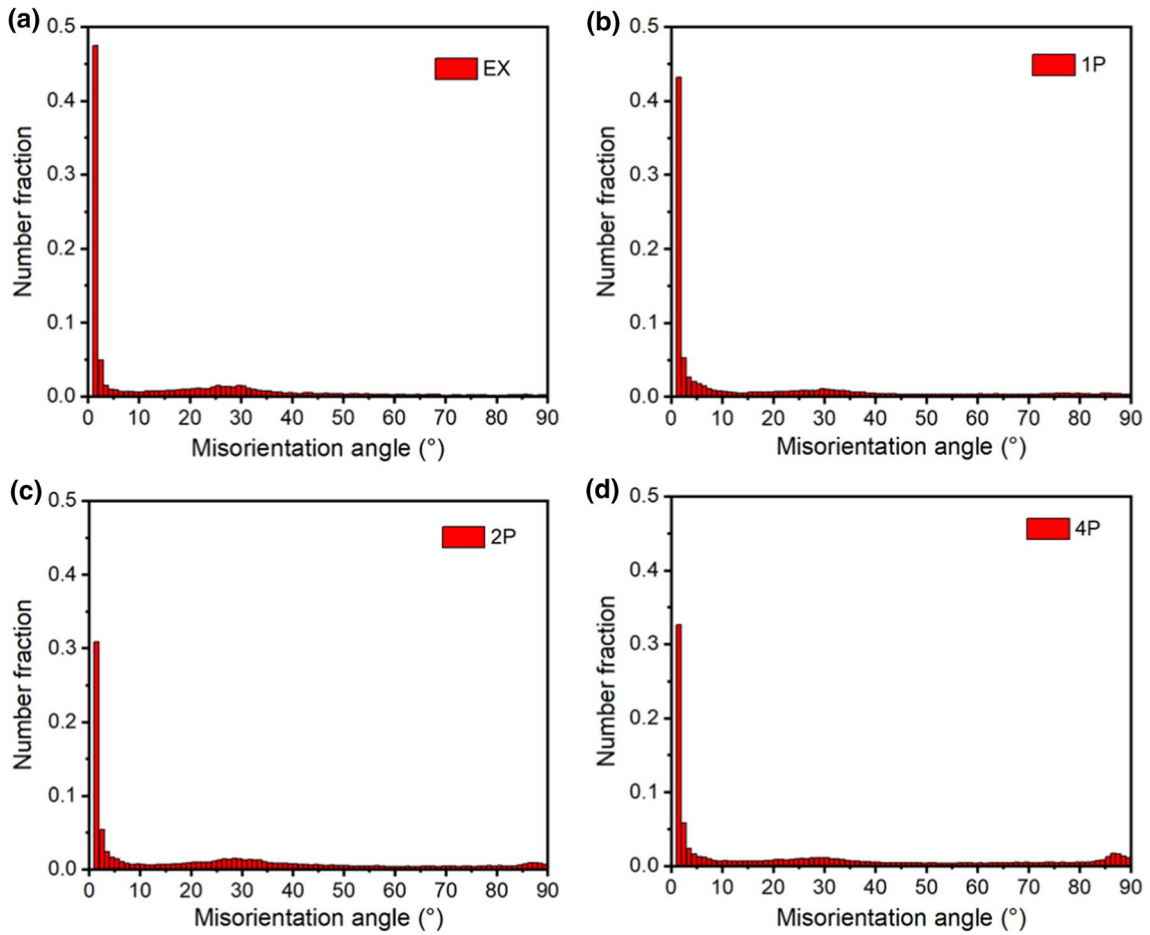


Fig. 11 Misorientation distribution of deformed Mg–6Zn–1Mn alloy: **a** Ex; **b** 1P; **c** 2P; **d** 4P

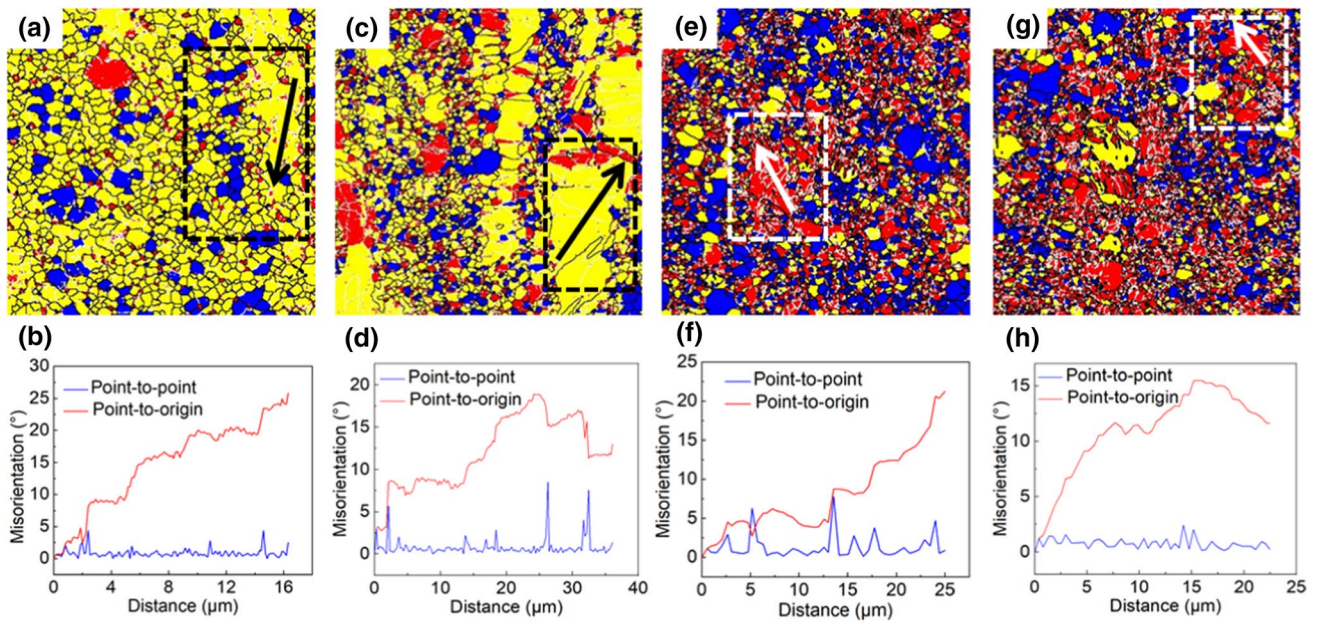
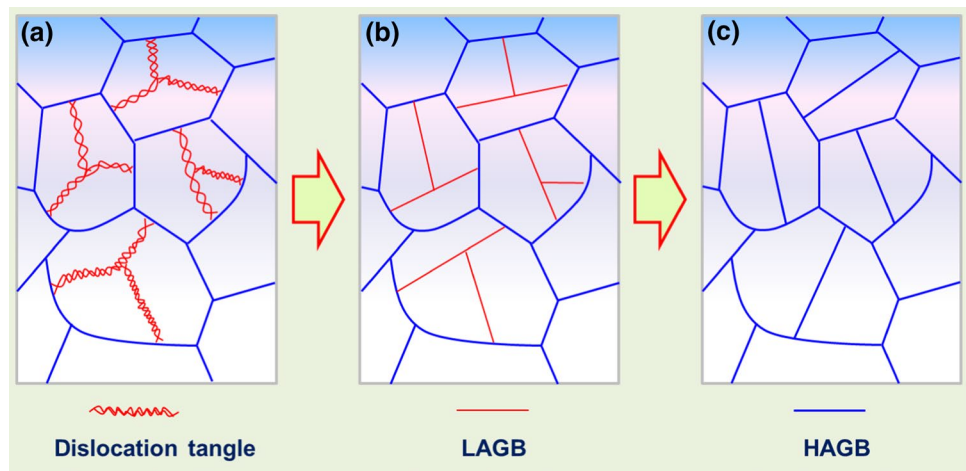


Fig. 12 The recrystallized region evolution image (**a**, **c**, **e**, **g**) and the local and cumulative misorientation (**b**, **d**, **f**, **h**) of deformed Mg–6Zn–1Mn alloys: **a**, **b** Ex; **c**, **d** 1P; **e**, **f** 2P; **g**, **h** 4P

Fig. 13 The schematic views of the CDRX behaviour for Mg–6Zn–1Mn alloy in this study



[14]. Finally, the $\{0001\}\langle -12-10 \rangle$ recrystallization texture is formed in the 4P sample (Fig. 14d). In general, the texture component of Mg alloys processed by ECAP deformation is related to shear deformation behavior and temperature. In the multi-pass ECAP deformation, the strain path and deformation pattern are complicated, which may lead to the formation of different textures. Kim et al. [35] have reported that the initial basal texture of the extruded AZ61 Mg alloy disappears after the 2 passes of ECAP (employing the route Bc and a temperature of 275 °C), and non-basal textures form with an increase in deformation. The grain orientation constantly changes during the entire process owing to the shear stress. Moreover, the processing temperature significantly influences the texture formation [6]. Different texture components are generated based on the interactions between the activation of the main slip and the DRX effect. Therefore, the texture evolution of the Mg–6Zn–1Mn alloy developed herein can be attributed to the DRX effect and the slip system activation.

The basal deformation texture in the extruded alloy splits into two texture components after 1 pass of ECAP: $\{0001\}\langle -10-10 \rangle$ and $\{-12-10\}\langle -10-11 \rangle$. This indicates that a non-basal slip is activated in the 1 pass deformation. The DRX behavior exerts a slight effect on the texture formation during this time, which also can be confirmed by the small DRX fraction in Fig. 10. After 2 passes of ECAP, the basal deformation texture and basal recrystallization texture form in the Mg alloy. Tong et al. suggested that the formation of this unique texture component after 2 passes of ECAP deformation can be attributed to the activation of the prismatic slip system [14]. In this study, DRX induced by moderate deformation temperature and large accumulated strains also is the main reason for the texture generation in the 2P sample, particularly for the recrystallization texture. Their formation can be mainly attributed to the oriented nucleation and selective growth of the grains. The oriented nucleation theory indicates that some crystal lattices with

special orientations can act as nuclei of grains [36]. The orientation distribution of the DRX grains is determined by the crystal nuclei in the deformed matrix. Moreover, the selective growth theory suggests that GB migration occurs more easily in certain crystal nuclei, causing the rapid growth of these grains and the formation of a recrystallization texture [36]. In this study, grains with $\langle 01-10 \rangle // ED$ and $\langle -12-10 \rangle // ED$ orientations were more likely to form after 2 passes of ECAP. This can be further confirmed by the OIM image in Fig. 15 that the most of the DRX grains exhibit the orientation of $\langle 01-10 \rangle // ED$ and $\langle -12-10 \rangle // ED$. Prado et al. investigated the development of new orientations in the extruded AZ61 alloy under different annealing conditions, and the results indicated that grain grows upon moderate annealing, leading to a basal texture [10]. Therefore, the unique texture component formation in the 2P sample can be attributed mainly to the effect of DRX. With further ECAP deformation (4 passes), the partial grain orientations remained unchanged, exhibiting a combination of strong $\{0001\}\langle -12-10 \rangle$ and weak $\{0001\}\langle 01-10 \rangle$ texture.

5.1 Strengthening and ductility improvement mechanism

Table 4 lists the alloy composition, processing conditions, and mechanical properties of the ECAP processed Mg–6Zn–1Mn alloy developed herein and in other previous study. The investigations on the ECAP for the Mg–6Zn–1Mn alloy are rarely reported; therefore, the results of this study are mainly compared with other Mg alloys series. The high alloyed Mg alloys are selected for an effective comparison. It can be seen that the Mg–6Zn–1Mn alloy we developed has the best combination of the strength and ductility. The combination of the extrusion and direct ECAP is significant for the mechanical properties of the alloy developed herein. More importantly, the extrusion and ECAP processing in this study were conducted at the low temperature and moderate

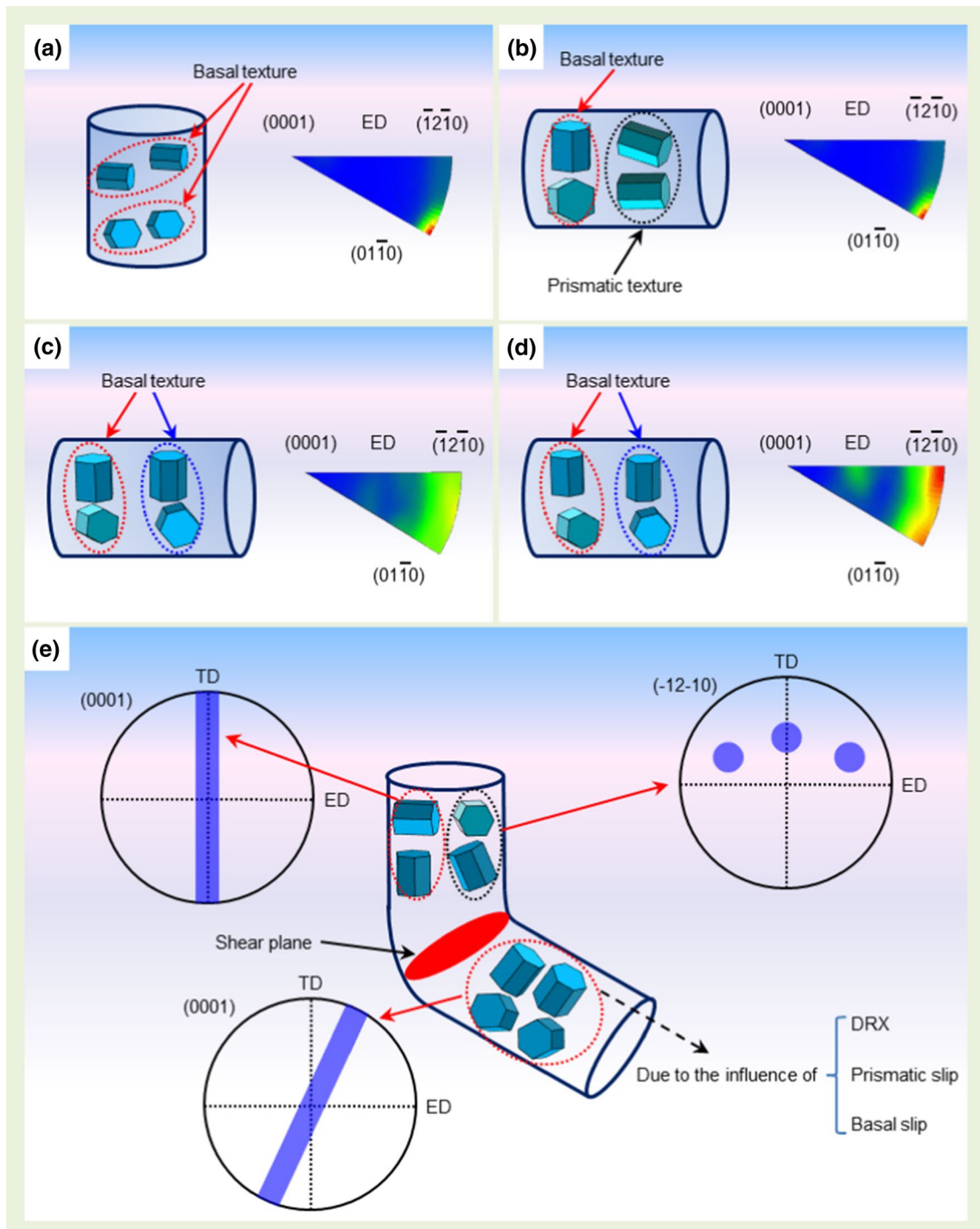


Fig. 14 The schematic views of the texture evolution mechanism: **a** Ex; **b** 1P; **c** 2P; **d** 4P; **e** the texture evolution from 1 to 2P sample

temperature, respectively. The low temperature extrusion was induced as a pre-treatment before ECAP to refine the microstructure of billets to improve the Mg–6Zn–1Mn alloy formability during ECAP. Furthermore, it can generate a heterogeneous grain structure with a low DRX fraction and a large fraction of sub-grains in the alloy. Subsequently,

moderate temperature ECAP was conducted to further optimize the grain size distribution, texture component, and dislocation density. Generally, ECAP is an effective grain refinement method involving the application of severe plastic deformation [20]. When processed using ECAP, the YS for materials decreases gradually while the EL tends to increase,

Fig. 15 **a** The recrystallized region image of the 2P sample; **b** OIM image of the 2P sample

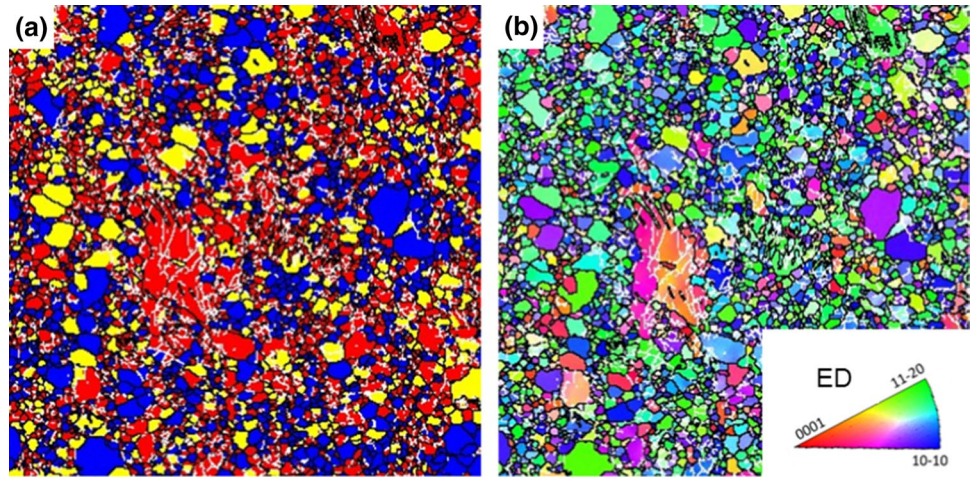


Table 4 Tensile properties of the Mg alloys prepared by the different temperature ECAP

| Alloy composition (wt%) | Processing conditions | Tensile properties | | | Refs |
|----------------------------------|--|--------------------|-----------|--------|-----------|
| | | YS (MPa) | UTS (MPa) | EL (%) | |
| Mg–6Zn–1Mn | As-cast + 420 °C /24 h + extruded at 260 °C + 2 passes ECAP (300 °C) | ~281 | ~306 | ~20.6 | This work |
| Mg–6Zn–0.5Ca–0.3Mn | As-cast + 400 °C /2 h + extruded at 300 °C + 2 passes ECAP (300 °C) | ~228 | ~303 | ~23.5 | [14] |
| Mg–5Y | As-cast + 530 °C /8 h + extruded at 300 °C + 3 passes ECAP (350 °C) | ~236 | ~271 | ~21.9 | [28] |
| Mg–2.9Gd–1.5Nd–0.3Zn–0.3Zr | As-cast + 520 °C /16 h + 4 passes ECAP (37.5 °C) | ~208 | ~260 | ~22 | [30] |
| Mg–6Al–1Zn | As-extruded + 350 °C /4 h + 4 passes ECAP (100 °C) | ~300 | ~360 | ~7 | [29] |
| Mg–6Al–1Zn | As-extruded + 350 °C /4 h + 4 passes ECAP (150 °C) | ~235 | ~325 | ~11 | [29] |
| Mg–6Al–1Zn | As-extruded + 350 °C /4 h + 4 passes ECAP (200 °C) | ~200 | ~310 | ~17.5 | [29] |
| Mg–6.08Zn–0.56Zr | As-cast + 430 °C /16 h + 4 passes ECAP (300 °C) | ~189 | ~311 | ~16.3 | [13] |
| Mg–8.4Li | As-cast + 2 passes ECAP (350 °C) | ~175 | ~186 | ~16 | [20] |
| Mg–8.4Li–3(Al–12Si)–1(Al–5Ti–1B) | As-cast + 2 passes ECAP (350 °C) | ~170 | ~243 | ~16.7 | [20] |
| AZ91 | As-extruded + 415 °C /20 h + 4 passes ECAP (300 °C) | ~220 | ~361 | ~12.6 | [37] |
| ZE41A | As-rolled + 4 passes ECAP (350 °C, 300 °C, 270 °C, and 240 °C, respectively) | ~321 | ~336 | ~6.2 | [38] |

presenting a reversed Hall–Petch effect [14]. This can be mainly attributed to the effect of grain, second phase, and texture. In this study, the changes in the YS during the ECAP process can be divided into two stages. At the first stage, the YS for the 1P sample increases slightly. With further deformation, the YS basically maintain a value of 281 MPa. In contrast, the EL first increases and then decreases during the entire deformation process. Among the analyzed samples, the 2P sample exhibits excellent comprehensive mechanical properties with the $YS \times EL$ value equal to 5.8, which is obtained by 2 passes ECAP deformation. The contribution of YS for the samples in this study can be expressed as follows:

$$\sigma_{ys} = \sigma_0 + \sigma_{gb} + \sigma_d + \sigma_p \quad (1)$$

where σ_{ys} is the YS, σ_0 can be interpreted as the YS of single crystal with the value of 50 MPa [39], σ_{gb} is the contribution of GBs strengthening, σ_d represents the dislocation strengthening, σ_p is the YS contribution of second phases.

Grain refinement is significant for the improvement of mechanical properties for Mg alloys [1, 4, 40, 41]. In this study, the size discrepancy between grains keeps shrinking with the processing of ECAP deformation. The average grain size of the ECAP processed samples was slightly larger than that of the extruded alloy. More GBs can effectively hinder the dislocation slip. Based on the Hall–Petch relationship, larger grain size will lead to lower YS. However, this trend is opposite to with the results obtained for the as-developed ECAP alloys. Therefore, other factors, such as the second phases and dislocation should also be considered.

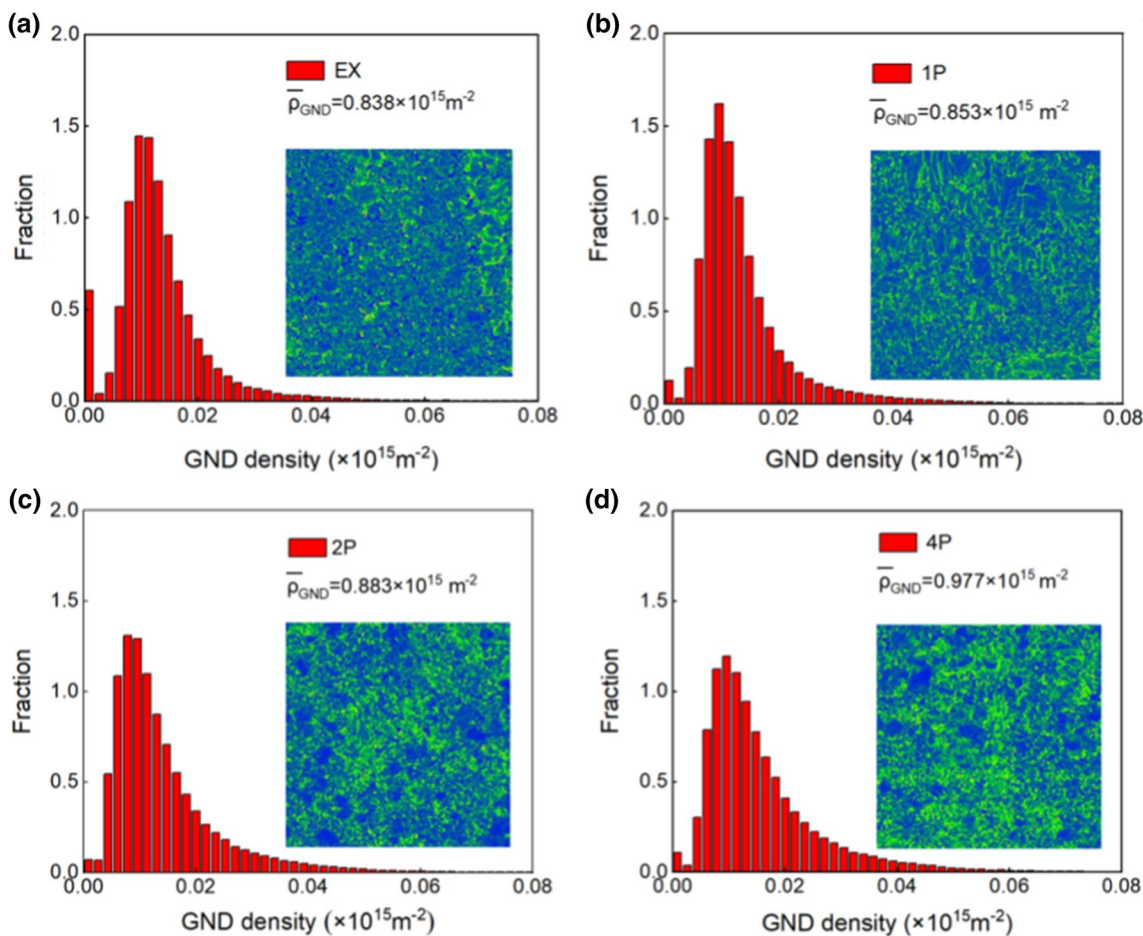


Fig. 16 The KAM image and distribution of ρ_{GND} for deformed Mg–6Zn–1Mn alloys: **a** Ex; **b** 1P; **c** 2P; **d** 4P

With the ECAP deformation, the more uniform and refined phases are formed in the samples, which can prevent dislocation movement and increase the YS of the materials. This also can be confirmed by our previous study, the uniformly distributed nanoparticles are achieved by the extreme plastic deformation, and the obvious enhancement of YS for Mg–Zn–Ca alloy is obtained as last [34]. In addition, the kernel average misorientation (KAM) images and ρ_{GND} distribution of the deformed Mg–6Zn–1Mn alloys in this study are shown in Fig. 16. With increase in ECAP deformation, a slight increase in the density of GNDs is observed, while maintaining the same order of magnitude. This suggests that the contribution of the dislocation to the YS is similar for the four samples.

Based on the above analysis, the quantitative calculations of GBs strengthening and dislocation strengthening contribution on YS are conducted, respectively. The GBs strengthening can be express as:

$$\sigma_{gb} = kd^{-1/2} \tag{2}$$

where k is the Hall–Petch relationship slope. For the pure Mg processed by hot extrusion, the k value is $157 \text{ MPa } \mu\text{m}^{1/2}$

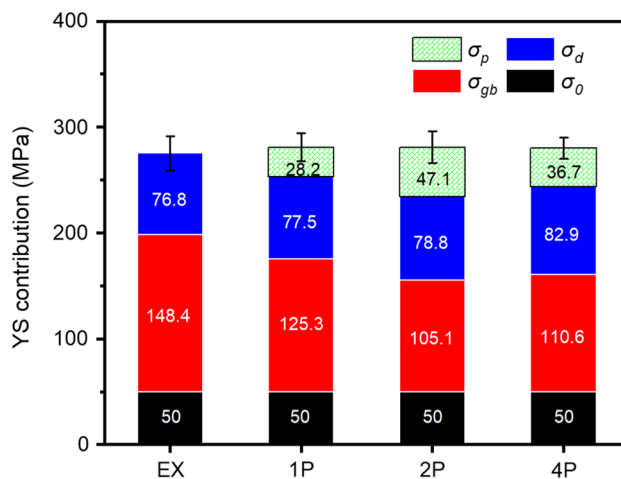


Fig. 17 The yield strength contribution of the different strengthening methods for deformed Mg–6Zn–1Mn alloys (the error range in the figure represents the total error of the sum of different strengthening mechanism)

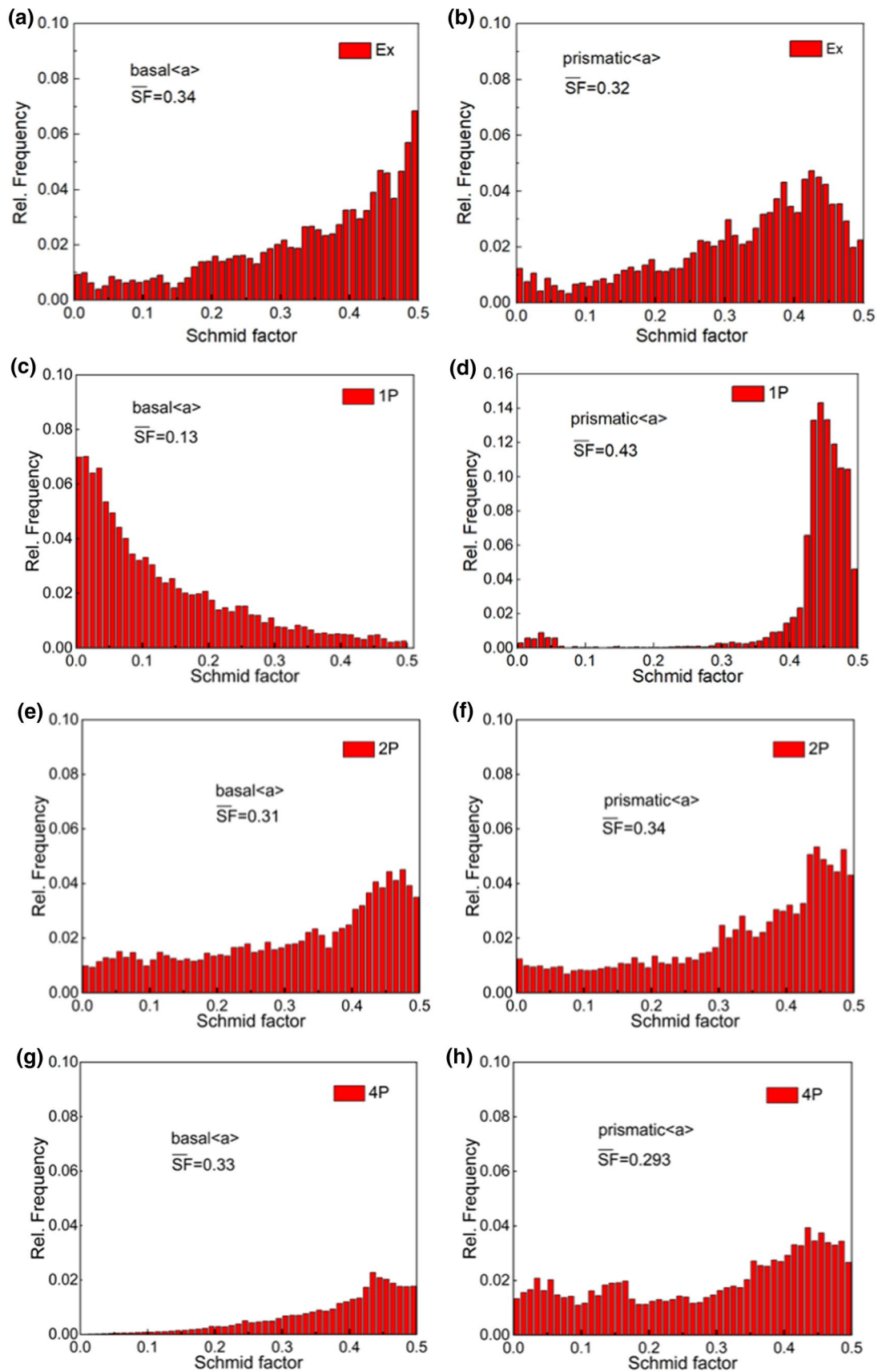


Fig. 18 SF distribution of Mg-6Zn-1Mn alloys: (a, c, e, g) {0001}<11-20> SF distribution; (b, d, f, h) {1-100}<11-20> SF distribution; a, b Ex; c, d 1P; e, f 2P; g, h 4P

[40]. And d denotes the average grain diameter.

Moreover, the contribution of dislocation on the YS can be calculated according to the following equation:

$$\sigma_d = M\alpha Gb\sqrt{\rho} \quad (3)$$

where M is the average Taylor factor with the value of ~ 2.5 for simplicity, α is a constant with the value of ~ 0.2 , G is the shear modulus with the value of ~ 17 GPa, and b is the Burgers vector with the value of ~ 0.3196 nm for Mg alloys. Considering the most of dislocations are GNDs induced by non-uniform deformation. Therefore, the GNDs were used to calculate the contribution of dislocations to the YS.

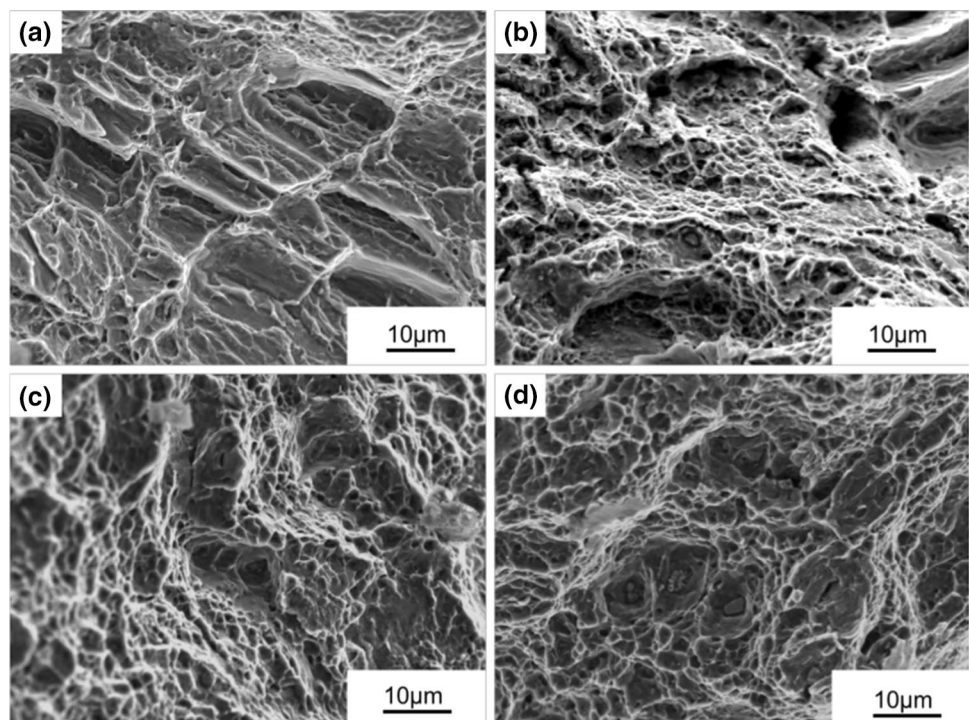
The contributions of the different strengthening mechanisms to the YS are shown in Fig. 17. The σ_0 is 50 MPa for the four samples. No significant difference is observed in the dislocation strengthening of the samples. Moreover, the extruded alloy possesses the smallest average grain size, resulting in the highest GBs strengthening value of 148.4 MPa. The 2P sample exhibits a minor GBs contribution of 105.1 MPa. In addition, the strengthening of the second phase contributes significantly to the YS, particularly for the 2P samples.

Figure 18 shows the SF distribution and average values of SF for the basal $\langle a \rangle$ slip and prismatic $\langle a \rangle$ slip for the ECAP processed samples. The extruded alloy shows a higher basal $\langle a \rangle$ slip SF with an average value of 0.34, corresponding to lower YS. The 1P sample exhibits a lower basal $\langle a \rangle$ slip SF with an average value of 0.13, indicating that basal

$\langle a \rangle$ slip is difficult to activate. However, owing to the heterogeneous grain structure, the plastic deformation of fine grains is easily activated by the stress accumulation of large grains. The 2P and 4P samples exhibit a higher basal $\langle a \rangle$ SF values of 0.31 and 0.33, respectively, indicating that most grains are in orientations where deformation occurs easily. Worthy of note is that a more homogeneous microstructure is obtained after 2 and 4 passes ECAP deformation. This is beneficial for delaying plastic deformation, leading to the enhancement of the YS. Therefore, the high strength of the as-developed Mg–6Zn–1Mn alloy can be mainly attributed to the effects of grains, dislocations, and second phases.

More importantly, the high strength Mg alloy processed by 2 passes ECAP also achieves an excellent ductility of $\sim 20.6\%$. This indicates that the more slip system may be activated in the tensile test, and stress concentration does not easily occur in the alloy. Therefore, the excellent ductility can be attributed to the following aspects. (i) The ductility of Mg alloys is closely related to the activation of the non-basal slip [2]. As observed in Fig. 18, the higher prismatic $\langle a \rangle$ slip SF of the 2P samples also indicates that the non-basal slip can be easily activated, which promotes the migration of dislocations. (ii) The 2P sample has a higher degree of DRX region with a randomized texture, which can more easily accommodate plastic strain. This is beneficial for the ductility. (iii) The highly uniform microstructure can delay the premature failure behavior, resulting in excellent ductility. Figure 19 shows an SEM image of the fracture surface of the deformed Mg–6Zn–1Mn alloy. Numerous cleavage planes

Fig. 19 SEM images of tensile fracture surface for deformed Mg–6Zn–1Mn alloy: **a** Ex; **b** 1P; **c** 2P; **d** 4P



and cleavage steps are present in the extruded alloy, corresponding to a low EL. With increasing ECAP deformation, the number of cleavage planes and cleavage steps decreases, while substantial and uniform dimples appear on the fracture surface, suggesting ductile fracture characteristics.

6 Conclusion

In summary, a strength-ductility synergy Mg–6Zn–1Mn alloy with $YS \times EL$ of 5.8 was developed by low temperature extrusion and moderate temperature ECAP (2 passes) deformation. The $YS \times EL$ value of the as-developed alloy is among the highest $YS \times EL$ values for similarly alloyed Mg alloys processed using ECAP and is obtained using minimum ECAP passes. The microstructures and tensile mechanical properties of the samples were investigated. The main conclusions drawn are as follows:

1. ECAP altered the microstructure of the Mg–6Zn–1Mn alloy, and uniformly distributed grains, second phases, and high-density dislocations were obtained for the 2P sample.
2. CDRX dominates the DRX mechanism during the entire deformation process.
3. Because of the dominant effect of DRX introduced by moderate temperature ECAP, a weak basal texture was formed in the 2P sample.
4. GB, dislocation, and second phase strengthening are the primary reasons for the high YS of the 2P sample. Significantly, the excellent ductility is primarily related to the uniform microstructure, weak basal texture, and high basal $\langle a \rangle$ slip and prismatic $\langle a \rangle$ slip SF.

Acknowledgements The authors gratefully acknowledge the financial supports from the Hongliu first-class discipline construction plan of Lanzhou University of Technology.

Declarations

Conflict of interest The authors declare that they have no known competing financial interests or personal relationships that could have appeared to influence the work reported in this paper.

References

1. R.G. Li, H.R. Li, D.Y. Zhao, Y.Q. Dai, D.Q. Fang, J.H. Zhang, L. Zong, J. Sun, *Mater. Sci. Eng. A* **780**, 139193 (2020)
2. H.C. Pan, D.S. Xie, J.R. Li, H.B. Xie, Q.Y. Huang, Q.S. Yang, G.W. Qin, *Mater. Res. Lett.* **9**, 329 (2021)
3. H.C. Pan, R. Kang, J.R. Li, H.B. Xie, Z.R. Zeng, Q.Y. Huang, C.L. Yang, Y.P. Ren, G.W. Qin, *Acta Mater.* **186**, 278 (2020)
4. H. Lv, L. Li, Z.Z. Wen, C.R. Liu, W. Zhou, X. Bai, H.L. Zhong, *Mater. Sci. Eng. A* **833**, 142521 (2022)
5. Z. Yang, C. Xu, T. Nakata, S. Kamado, *Mater. Sci. Eng. A* **800**, 140330 (2021)
6. X. Zhao, S.C. Li, Y.S. Zheng, Z.R. Liu, K. Chen, J.M. Yu, Z.M. Zhang, S.Q. Zheng, *J. Alloys Compd.* **883**, 160871 (2021)
7. D.D. Zhang, C.M. Liu, S.N. Jiang, Y.H. Gao, Y.C. Wan, Z.Y. Chen, *Mater. Sci. Eng. A* **856**, 143990 (2022)
8. Q. Xu, A.B. Ma, Y.H. Li, J.P. Sun, Y.C. Yuan, J.H. Jiang, C.Y. Ni, *J. Magnes. Alloys* **8**, 192 (2020)
9. R.S. Pei, Y.C. Zou, M. Zubair, D.Q. Wei, T. Al-Samman, *Acta Mater.* **233**, 117990 (2022)
10. M.T. Pérez-Prado, O.A. Ruano, *Scr. Mater.* **48**, 59 (2003)
11. H. Yan, X.H. Shao, H.P. Li, R.S. Chen, H.Z. Cui, E.H. Han, *Scr. Mater.* **207**, 114257 (2022)
12. Z.Q. Yang, A.B. Ma, B.Q. Xu, J.H. Jiang, H.R. Wu, J.P. Sun, *Mater. Sci. Eng. A* **841**, 143023 (2022)
13. Y.C. Yuan, A.B. Ma, X.F. Gou, J.H. Jiang, G. Arhin, D. Song, H. Liu, *Mater. Sci. Eng. A* **677**, 125 (2016)
14. L.B. Tong, J.H. Chu, W.T. Sun, Z.H. Jiang, D.N. Zou, S.F. Liu, S. Kamado, M.Y. Zheng, *J. Magnes. Alloys* **9**, 1007 (2021)
15. J. Horky, K. Bryła, M. Krystian, G. Mozdzen, B. Mingler, L. Sajti, *Mater. Sci. Eng. A* **826**, 142002 (2021)
16. H. Liu, H. Huang, Y. Zhang, Y. Xu, C. Wang, J.P. Sun, J.H. Jiang, A.B. Ma, F. Xu, J. Bai, *J. Alloys Compd.* **811**, 151987 (2019)
17. K. Yan, J. Bai, H. Liu, Z.Y. Jin, *J. Magnes. Alloys* **5**, 336 (2017)
18. M.A. Afifi, Y.C. Wang, P.H.R. Pereira, Y.W. Wang, S.K. Li, Y. Huang, T.G. Langdon, *Mater. Sci. Eng. A* **712**, 146 (2018)
19. W.W. Lei, H. Zhang, *Mater. Lett.* **271**, 127781 (2020)
20. X.W. Liu, L.P. Bian, F. Tian, S.J. Han, T. Wang, W. Liang, *Mater. Charact.* **188**, 111910 (2022)
21. Y.T. Fu, J.P. Sun, Z.Q. Yang, B.Q. Xu, J. Han, Y.F. Chen, J.H. Jiang, A.B. Ma, *Mater. Charact.* **165**, 110398 (2020)
22. K.B. Nie, Z.H. Zhu, K.K. Deng, J.G. Han, *J. Magnes. Alloys* **8**, 676 (2020)
23. D.L. Yu, D.F. Zhang, J. Sun, Y.X. Luo, J.Y. Xu, H.J. Zhang, F.S. Pan, *Mater. Sci. Eng. A* **662**, 1 (2016)
24. D.L. Yu, D.F. Zhang, Q.W. Dai, W. Lan, J. Peng, J.Y. Xu, F.G. Qi, F.S. Pan, *Mater. Sci. Eng. A* **711**, 624 (2018)
25. J. Peng, X.S. Tong, S.L. Shang, F.S. Pan, *Rare Metal Mater. Eng.* **42**, 1627 (2013)
26. C.Q. Liu, X.H. Chen, J. Chen, A. Atrens, F.S. Pan, *J. Magnes. Alloys* **9**, 1081 (2021)
27. H.F. Zhang, Y.T. Ding, L. Jian, Y. Shen, J.J. Chen, Y.B. Gao, *Mater. Rep.* **36**, 172 (2022)
28. W. Yang, G.F. Quan, B. Ji, Y.F. Wan, H. Zhou, J. Zheng, D.D. Yin, *J. Magnes. Alloys* **10**, 195 (2022)
29. Z.H. Shan, J. Yang, J.F. Fan, H. Zhang, Q. Zhang, Y.C. Wu, W.G. Li, H.D. Dong, B.S. Xu, *J. Magnes. Alloys* **9**, 548 (2021)
30. Z.Z. Gui, F. Wang, J.Y. Zhang, D.X. Chen, Z.X. Kang, *J. Magnes. Alloys* **10**, 239 (2022)
31. X. Zhao, S.C. Li, Z.M. Zhang, P.C. Gao, S.L. Kan, F.F. Yan, *J. Magnes. Alloys* **8**, 624 (2020)
32. K.K. Guo, M.Y. Liu, J.F. Wang, Y.F. Sun, W.Q. Li, S.J. Zhu, L.G. Wang, S.K. Guan, *J. Magnes. Alloys* **8**, 873 (2020)
33. Y.W. Gui, L.X. Ouyang, Y.J. Cui, H.K. Bian, Q.A. Li, A. Chiba, *J. Magnes. Alloys* **9**, 456 (2021)
34. H.F. Zhang, Y.T. Ding, R.M. Li, Y. Shen, J. Lei, *Mater. Sci. Eng. A* **853**, 143733 (2022)
35. W.J. Kima, S.I. Hong, Y.S. Kim, S.H. Min, H.T. Jeong, J.D. Lee, *Acta Mater.* **51**, 3293 (2003)
36. Z.H. Chen, *Wrought Magnesium Alloy*, 1nd edn. (Chemical Industry Press, 2005), pp. 335–336.
37. B.Q. Xu, J.P. Sun, Z.Q. Yang, L.R. Xiao, H. Zhou, J. Jin, H. Liu, Y.N. Wu, Y.C. Yuan, X.R. Zhou, D. Song, J.H. Jiang, A.B. Ma, *Mater. Sci. Eng. A* **780**, 139191 (2020)
38. K. Bryła, *Mater. Sci. Eng. A* **772**, 138750 (2020)

39. X.P. Zhang, S. Castagne, C.F. Gu, X.F. Luo, *J. Mater. Sci.* **46**, 1124 (2011)
40. H.H. Yu, Y.C. Xin, M.Y. Wang, Q. Liu, *J. Mater. Sci. Technol.* **34**, 248 (2018)
41. L. Li, C.C. Zhang, H. Lv, C.R. Liu, Z.Z. Wen, J.W. Jiang, *J. Magnes. Alloys* **10**, 249 (2022)

Springer Nature or its licensor (e.g. a society or other partner) holds exclusive rights to this article under a publishing agreement with the author(s) or other rightsholder(s); author self-archiving of the accepted manuscript version of this article is solely governed by the terms of such publishing agreement and applicable law.

Publisher's Note Springer Nature remains neutral with regard to jurisdictional claims in published maps and institutional affiliations.